coatings

MDPI

Article

Study on Mechanism of Microstructure Refinement by Ultrasonic Cavitation Effect

Chang Li *, Shuchao Li, Jiabo Liu, Yichang Sun, Yuhao Wang and Fanhong Kong

School of Mechanical Engineering and Automation, University of Science and Technology Liaoning, Anshan 114051, China
* Correspondence: lichang2323-23@163.com

Abstract: During the solidification process of the alloy, the temperature lies in the range between the solid-phase line and the liquidus. Dendrite growth exhibits high sensitivity to even slight fluctuations in temperature, thereby significantly influencing the tip growth rate. The increase in temperature can result in a reduction in the rate of tip growth, whereas a decrease in temperature can lead to an augmentation of the tip growth rate. In cases where there is a significant rise in temperature, dendrites may undergo fracture and subsequent remelting. Within the phenomenon of ultrasonic cavitation, the release of internal energy caused by the rupture of cavitation bubbles induces a substantial elevation in temperature, thereby causing both dendrite remelting and fracture phenomena. This serves as the main mechanism behind microstructure refinement induced by ultrasonic cavitation. Although dendrite remelting and fracture exert significant influences on the solidification process of alloys, most studies primarily focus on microscopic characterization experiments, which fail to unveil the transient evolution law governing dendrite remelting and fracture processes. Numerical simulation offers an effective approach to address this gap. The existing numerical models primarily focus on predicting the dendrite growth process, while research on remelting and fracture phenomena remains relatively limited. Therefore, a dendrite remelting model was established by incorporating the phase field method (PFM) and finite element difference method (FDM) into the temperature-induced modeling, enabling a comprehensive investigation of the entire process evolution encompassing dendrite growth and subsequent remelting.

Keywords: cavitation effect; ultrasonic vibration; dendrite remelting; regrowth; thinning tissue

Citation: Li, C.; Li, S.; Liu, J.; Sun, Y.; Wang, Y.; Kong, F. Study on Mechanism of Microstructure Refinement by Ultrasonic Cavitation Effect. *Coatings* **2024**, *14*, 1462. https://doi.org/10.3390/coatings14111462

Academic Editor: Avik Samanta

Received: 30 September 2024
Revised: 13 November 2024
Accepted: 14 November 2024
Published: 17 November 2024

1. Introduction

The main driving factors governing the process of dendrite remelting are induced solute concentration and temperature variations. By integrating cellular automata (CA) with the finite volume method (FVM) [1], Neng Ren successfully simulated the growth and remelting process of dendrites induced by solute. The modeling takes into account critical conditions for mechanical breakage, as well as dendrite melting and breakage caused by convective flow and solute segregation. The phenomenon of dendrite melting induced by temperature plays a crucial role in the ultrasonic-assisted laser cladding process. Upon the bursting of ultrasonic cavitation bubbles, a substantial amount of heat is released, leading to an elevation in the local temperature of the molten pool and subsequently initiating dendrite melting [2]. Dendrite remelting is a multifaceted phenomenon occurring during the metal solidification process, encompassing three pivotal stages: liquefaction, fragmentation, and regrowth. This study investigates the dendrite melting and fracture phenomena, as well as the subsequent regrowth of fractured dendrites during temperature elevation. By simulating the regrowth process of dendrites at varying melting degrees, a comprehensive investigation was conducted on the newly formed dendritic structures.

Ultrasonic cavitation is a theoretical framework proposed based on the phenomenon of acoustic cavitation, encompassing the dynamic processes of bubble formation, vibration,

and rapid rupture induced by ultrasonic waves [3]. The earliest documented observations of cavitation can be traced back to 1895 when Thornycroft and Barnaby reported their findings at the Engineering Society [4]. In 1917, Rayleigh formulated the inaugural mathematical model of cavitation behavior exhibited by a solitary bubble in an incompressible liquid, which is now recognized as the Rayleigh–Plesset equation [5]. In 1935, Frenzel and Schulze observed that the immediate collapse of bubbles induced by a strong ultrasonic field in water resulted in an emission characterized by high temperature and pressure [6]. Furthermore, in 1950, Neppiras and Noltingk discreetly employed early computer technology to solve the cavitation bubble equation and subsequently published the pioneering numerical model for simulating cavitation bubble behavior [7]. These seminal studies have established a solid groundwork for the practical utilization of the cavitation effect in engineering.

The phenomenon of acoustic cavitation can be observed in any liquid when exposed to ultrasonic waves. For instance, the liquid contains a suspended bubble that exhibits expansion and contraction in response to a specific intensity of ultrasonic waves [8]. This phenomenon, known as acoustic cavitation, involves the continuous oscillation, expansion, and rupture of the bubble. The cavitation bubble can be considered an insulating sphere possessing various forms of energy, such as surface tension from the liquid, kinetic energy, and energy imparted by sound waves. Upon the bursting of the cavitation bubble, a conversion of energy occurs, resulting in the formation of high-temperature and high-pressure microjets. The temperature elevation associated with the burst of the cavitation bubble is directly correlated to its radius, as shown in Figure 1 [9]. Acoustic cavitation plays a pivotal role in enhancing the microstructure, particularly during laser cladding processes where the temperature rise induced by cavitation facilitates dendrite remelting and subsequent microstructure refinement.

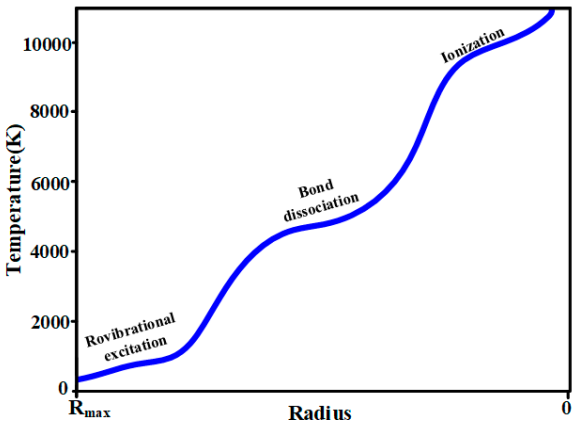

Figure 1. Relationship between cavitation bubble rupture temperature and bubble radius.

To describe the motion of a single cavitation bubble, the corresponding motion equation was established based on the Noltingk–Neppiras model [7]:

$$\rho_L\left(RR_{tt}+\frac{3}{2}R_t^2\right)=\left(P_0+\frac{2\sigma_F}{R_a}\right)\left(\frac{R_a}{R}\right)^{3\gamma}+P_v-\frac{2\sigma_F}{R_a}-P_0+P_m\sin(\omega t) \quad (1)$$

where R is the cavitation bubble radius, R_t and R_{tt} are the first and second derivatives of the cavitation radius concerning time, P_0 = 101 kPa is the static pressure inside the bubble, σ_F is the surface tension of the melt, R_a is the initial bubble radius, and P_v = 327 kPa is the saturated vapor pressure.

The moment of cavitation bubble rupture releases a significant amount of energy, resulting in a substantial increase in temperature and pressure. The highest temperature

rise (T_{max}) and maximum pressure (P_{max}) generated during the collapse can be determined using the following formula:

$$\begin{cases} T_{\max} = T_0 \left[\frac{P_0(\gamma-1)}{P_v} \right] \\ P_{\max} = P_v \left[\frac{P_m(\gamma-1)}{P_v} \right]^{\frac{\gamma}{\gamma-1}} \end{cases} \quad (2)$$

where T_0 is the temperature in the molten pool, P_0 is the external pressure when the bubble bursts, and γ is the specific heat capacity of the gas in the bubble.

The calculation reveals that the collapse of the cavitation bubble can result in a maximum temperature rise (T_{max}) of 10^4 K and a maximum pressure (P_{max}) of 10^4 atm [10].

Cavitation-generated high-pressure shock waves can elevate the local melt's melting point [11]. The temperature increase is primarily influenced by pressure and enthalpy, and ΔT can be determined using the Clausius–Clapeyron equation:

$$\Delta T = \frac{T_M \Delta V}{\Delta H} \Delta P \quad (3)$$

where ΔV and ΔH are the volume and enthalpy changes during solidification, respectively, and ΔP is the high-pressure shock wave generated by the cavitation phenomenon.

Currently, research on the mechanism of ultrasonic cavitation in refining grain can be broadly categorized into two theories. One theory suggests that local supercooling induced by ultrasonic cavitation plays a pivotal role in grain refinement, which has been substantiated through practical applications [12,13]. The other theory proposes that the high temperature and pressure environment generated by ultrasonic cavitation facilitates microstructure refinement [14]. According to the phenomenon of ultrasonic cavitation, this study investigates the enhancement of microstructure through dendrite remelting at elevated temperatures.

2. Experimental Equipment and Materials

In this study, the accuracy of numerical simulation is verified by observing the specimen after laser cladding. The experimental setup utilized a disk laser (TruDisk4002) manufactured by TRUMPF (Ditzingen, Germany), operating at a power level of 1600 W with a minimum fiber diameter of 0.2 mm and a laser wavelength of 1.030 μm, the laser scanning speed is 6 mm/s. The 45 steel was chosen as the substrate material, while 316 L powder served as the cladding material. The specimens (Figure 2) were longitudinally cut along the vertical scanning direction, followed by polishing and immersion in a 4% nitrate alcohol solution for corrosion testing. Metallographic analysis was performed using an optical microscope to examine the microstructure of the coating layer.

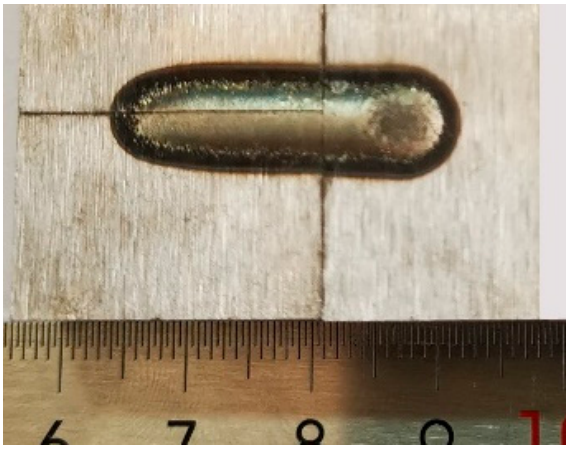

Figure 2. Cladding test block.

3. The Construction of the Phase Field Model

3.1. Free Energy Functional Phase Field Model

According to the Ginzburg–Landau free energy theory [15], in a closed system with volume Ω, the expression of the free energy functional F is:

$$F = \int_{\Omega} \left[f(\psi, e) + \frac{1}{2}\varepsilon_{\psi}^{2}(\nabla\psi)^{2} \right] d\Omega \tag{4}$$

where f is the free energy density, e is the internal energy of the system, and ε_{ψ} is the coefficient of the phase field gradient term, $\psi = 0$ is a solid, $\psi = 0$ is a liquid, $0 < \psi < 1$ indicates the mushy region.

According to the second law of thermodynamics, energy is conserved during solidification, and the free energy of the system exhibits a tendency to decrease over time ($Df \leq 0$). Formulas (5) and (6) can be derived based on the principles of minimum energy and irreversible dynamics:

$$\frac{\partial\psi}{\partial t} = -M_{\psi}\frac{\delta F}{\delta\psi} \tag{5}$$

$$\frac{\partial e}{\partial t} = \nabla\cdot\left(M_{e}\nabla\frac{\delta F}{\delta e} \right) \tag{6}$$

where M_{ψ} is the phase field parameter related to interfacial dynamics, and M_e is the phase field parameter related to thermal diffusion.

3.2. Phase Field Equation

The solidified alloy phase field equation was derived based on the free energy functional phase field model.

$$\frac{\partial\psi}{\partial t} = M_{\psi}\left(-\varepsilon_{\psi}^{2}\nabla^{2}\psi + \frac{\partial f(\psi, e)}{\partial\psi} \right) \tag{7}$$

According to the principle of classical thermodynamics [16], the variational equation of F in equilibrium must be satisfied.

$$\frac{\delta F}{\delta\psi} = \frac{\partial f}{\partial\psi} - \varepsilon_{\psi}^{2}\nabla^{2}\psi = 0 \tag{8}$$

The variation of the phase field parameter ψ along the normal direction at the interface can be mathematically described by the following equation.

$$\psi = \frac{1}{2}\left[1 + \tanh\left(\frac{n}{2\delta_{m}} \right) \right] \tag{9}$$

Based on Equation (9), it can be derived.

$$|\nabla\psi| = \frac{\partial\psi}{\partial n} = \frac{\psi(1-\psi)}{\delta_{m}} \tag{10}$$

$$\frac{\nabla\psi\nabla|\nabla\psi|}{|\nabla\psi|} = \frac{\partial^{2}\psi}{\partial n^{2}} = \frac{\psi(1-\psi)(1-2\psi)}{\delta_{m}^{2}} \tag{11}$$

The relationship between the phase field parameter ψ in the normal direction and the interface thickness δ_m can be determined through Equations (10) and (11). By substituting Equations (9)–(11) into the interface equation, we obtain the phase field control equation as follows:

$$\frac{1}{\mu_{k}}\frac{\partial\psi}{\partial t} = \Gamma\left[\nabla^{2}\psi - \frac{\psi(1-\psi)(1-2\psi)}{\delta_{m}^{2}} \right] + (T_{M} - T)\left[\frac{\psi(1-\psi)}{\delta_{m}} \right] \tag{12}$$

where μ_k is the kinetic coefficient, T_M is the melting temperature of the alloy, δ_m is the interface thickness, Γ is the Gibbs–Thomson coefficient, and m_L is the liquidus slope of the alloy solution.

According to the heat transfer equation, the temperature field equation can be expressed as follows [17]:

$$\frac{\partial \widetilde{T}}{\partial t} = \alpha_T \nabla^2 \widetilde{T} + \frac{L_m}{C_p} \frac{\partial P(\psi)}{\partial t} \tag{13}$$

where α_T is the thermal diffusion coefficient, L_m is the latent heat, C_p is the specific heat.

3.3. Interfacial Anisotropy

During the solidification process, the anisotropic interfacial energy at the solid–liquid interface dictates the preferred orientation of dendrite growth, wherein dendrites invariably propagate in the direction characterized by minimal interfacial energy. The anisotropy of the interface energy plays a pivotal role in both dendrite morphology evolution and interface stability [18]. The anisotropy ε of the interface is contingent upon the direction of the outward normal vector, with its enclosed angle being expressed as [19]:

$$\theta = \frac{\nabla \psi}{|\nabla \psi|} = \arctan\left(\frac{\partial \psi / \partial y}{\partial \psi / \partial x}\right) \tag{14}$$

$$\varepsilon = \bar{\varepsilon}\eta(\theta) = \bar{\varepsilon}(1 + \delta \cos(k_\varepsilon(\theta - \theta_0))) \tag{15}$$

where $\bar{\varepsilon}$ is the average value of anisotropic gradient energy coefficient [20]; δ is the anisotropy intensity, generally between 0.02~0.1; k_ε is the anisotropic modulus, usually 4 or 6, because the material simulated in this paper is FCC (face-centered cubic structure), $k_\varepsilon = 4$ [21]; θ is the angle between the main dendrite arm and the interface normal vector, and θ_0 is the initial angle defined when the dendrite begins to grow.

3.4. The Addition of Noise Disturbances

During the solidification process, the solid–liquid interface exhibits random fluctuations attributed to solute diffusion and heat flow. To enhance the accuracy of simulation results, noise disturbances are incorporated at the solid–liquid interface by introducing additional terms into the phase field equation [22]:

$$\frac{\partial \psi}{\partial t} \rightarrow \frac{\partial \psi}{\partial t} + 16 g'(\psi) \alpha r^* \tag{16}$$

where $g'(\psi)$ is the derivative of $g(\psi) = \psi^2(1 - \psi)^2$, alpha for disturbance intensity factor (with time), r^* for random number between 1 and +1. To ensure that the disturbance occurs at the interface, the influence of the noise term exists only in the range $0 \leq \psi \leq 0.5$ [23].

4. Phase Field Governing Equations and Boundary Conditions

4.1. Process Parameter Setting

Dendrite remelting refers to the phenomenon of dendrite remelting due to the increase in the surrounding temperature. To clearly describe the dendrite remelting process under ultrasonic cavitation, the non-isothermal phase field model derived by Kobayashi [24], Boettinger [25], and Zaeem [26] was adopted in this paper. The phase field governing equation and temperature field equation of this model are:

$$\begin{aligned} \frac{\tau_c}{\bar{\varepsilon}_m^2} \frac{\partial \psi}{\partial t} = & \left[\frac{\partial}{\partial x}\left(\frac{\partial \varepsilon^2(\theta)}{\partial \theta}\frac{\partial \psi}{\partial y}\right) - \frac{\partial}{\partial y}\left(\frac{\partial \varepsilon^2(\theta)}{\partial \theta}\frac{\partial \psi}{\partial x}\right) + \nabla \cdot \left(\varepsilon^2(\theta)\psi\right)\right] \\ & + \frac{1}{\bar{\varepsilon}_m^2}\psi(1-\psi)\left[\psi - \tfrac{1}{2} + M(T)\right] \end{aligned} \tag{17}$$

$$\frac{\partial \widetilde{T}}{\partial t} = \alpha_T \nabla^2 \widetilde{T} + \frac{L_m}{C_p} \frac{\partial \psi}{\partial t} \tag{18}$$

where τ_c and $\widetilde{\varepsilon}_m$ are phase field interface parameters, $\varepsilon(\theta)$ is the anisotropic of the solid–liquid interface ($\varepsilon(\theta)$ is a function of θ), $M(T)$ is the interface driving term in the phase field equation, C_p is the heat capacity at constant pressure, L_m is the latent heat, and $\widetilde{T}$ is the dimensionless temperature ($\widetilde{T} = (T - T_S)/(T_L - T_S)$) [27]. α_T is the thermal diffusion coefficient of a metal.

$$\alpha_T = \frac{l_0^2}{\tau} = \frac{k}{\rho C_p} \tag{19}$$

4.2. Boundary Conditions for Numerical Simulation

To accurately depict the growth behavior of the dendrite remelting process, the position of crystal nuclei was pre-set in this paper, as shown in Figure 3. The crystal nuclei are positioned at the bottom of the simulation domain, ensuring sufficient inter-nuclei spacing to facilitate the development of secondary dendrite arms. During the solution of the governing equations in the phase field model, it is assumed that these nucleation positions are solely influenced by growth dynamics rather than other external conditions. Therefore, the simulation domain boundary condition was set to zero flux boundary.

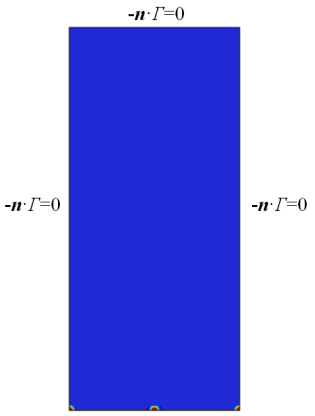

Figure 3. Nucleation positions and boundary conditions of dendrite remelting settings.

5. Numerical Simulation Results of Remelting and Regrowth Process

5.1. The Remelting Process of Dendrite Growth

The normal state of dendrite growth prior to the rise in ambient temperature is shown in Figure 4. The findings demonstrate that, due to interface anisotropy, the main dendrite arms exhibit growth in both horizontal and vertical directions, as shown in Figure 4a. Due to spatial constraints, the growth of main dendrites is impeded horizontally due to inhibition from neighboring dendrites, while vertical dendrites exhibit unrestricted growth, as shown in Figure 4b.

After a time step of 3000 Δt, the temperature surrounding the dendrites exhibits an increase, resulting in a gradual melting of the dendritic structure, as shown in Figure 5. The computational analysis reveals that at 3014 Δt, the lateral branches of the dendrites commence melting while the main axis of the dendrite displays a tendency to contract, as shown in Figure 5a. The melting process inhibits dendrite growth, resulting in the complete melting of some short lateral branches and a significant reduction in both the width and length of thick lateral branches, as shown in Figure 5b. The lateral branches that have not fully melted break at the root by 3030 Δt, while the main dendrite arms exhibit a distinct contraction trend, as shown in Figure 5c. The lateral branches of the dendrites are significantly dissolved at 3040 Δt, while clear indications of melting can also be observed in the main dendrite arms, as shown in Figure 5d. During the remelting process, the main dendrite arms exhibit a tendency to contract, leading to a reduction in branch width.

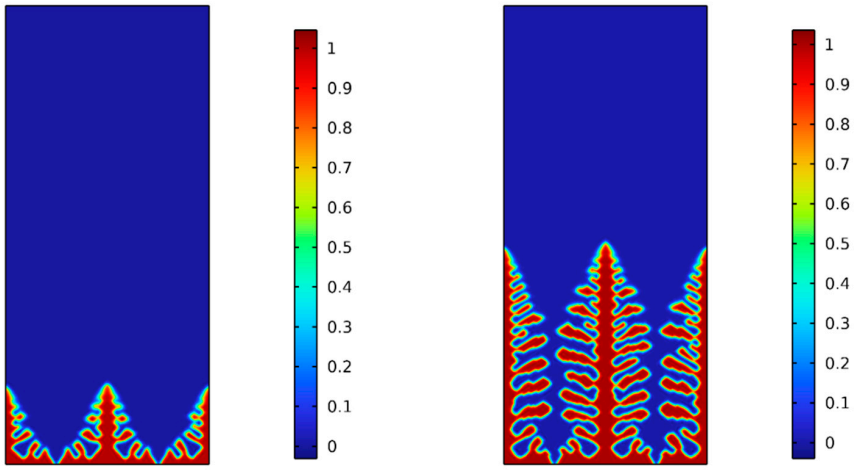

Figure 4. Normal dendrite growth in 3000 Δt; (**a**) dendrite morphology at 1000 Δt; and (**b**) dendrite morphology at 3000 Δt.

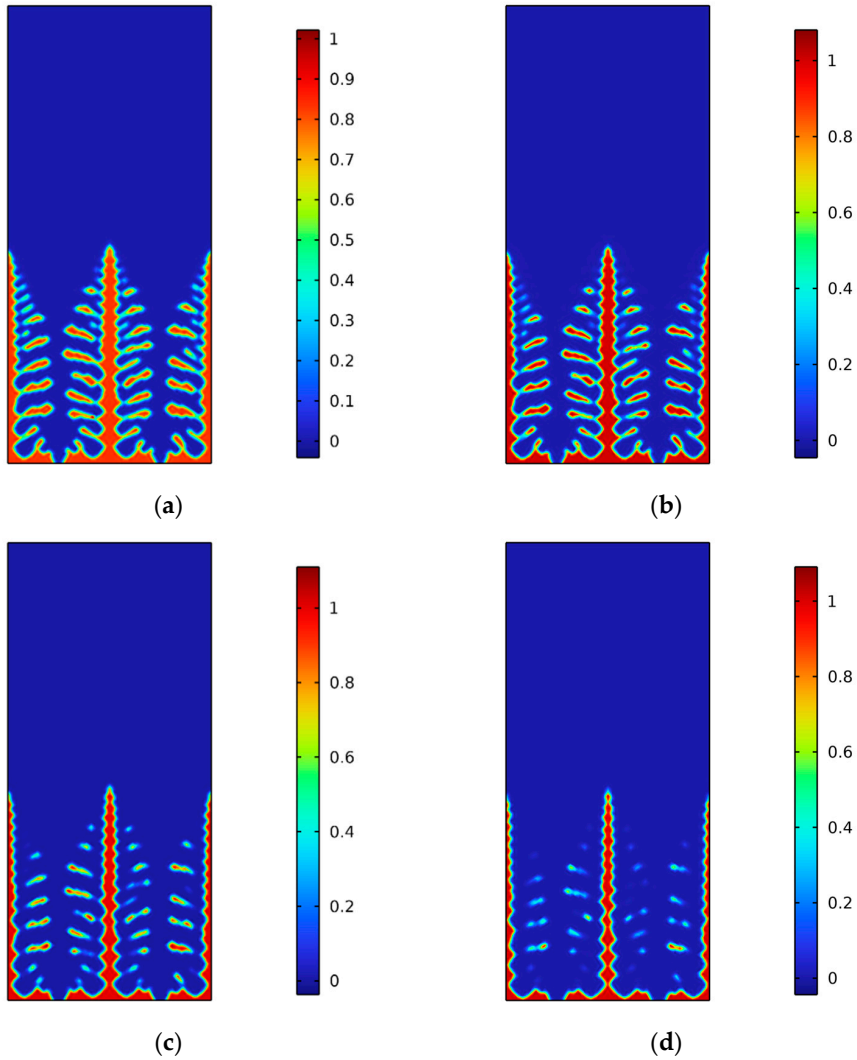

Figure 5. The process of large dendrite melting after 3000 Δt; (**a**) dendrite morphology at 3005 Δt; (**b**) dendrite morphology at 3020 Δt; (**c**) dendrite morphology at 3030 Δt; and (**d**) dendrite morphology at 3040 Δt.

5.2. Dendrite Regrowth Process in Which Lateral Branches Are Not Completely Melted

The temperature rise caused by the ultrasonic cavitation effect is limited and transient. The resulting thermal effects are not evenly distributed in space, resulting in different dendrite remelting degrees at different locations. The dendrites in close proximity to the cavitation center exhibit a pronounced degree of melting, potentially leading to complete liquefaction, whereas those located further away from the cavitation center display a minimal extent of melting. Therefore, under identical temperature gradients and latent heat conditions, the regrowth morphology of dendrites following remelting can exhibit distinct thinning characteristics due to variations in their melting points. To ensure the precision of the numerical simulation, certain assumptions were incorporated during the remelting dendrite regrowth simulation:

(1) The driving force of temperature undercooling during dendrite regrowth remains unchanged;
(2) The regrowth of adjacent dendrites is restricted by the boundary on both sides;
(3) Latent heat remained constant during dendrite regrowth.

In the initial stage of melting, the majority of the main dendrite arms remain intact, while a significant portion of their lateral branches undergo a process known as melting fracture, as shown in Figure 6a. This is because the dendrite melting process lasts for a short time, when the temperature drops after the lateral branch breaks, the melt is again suitable for the supercooling state of metal solidification. The fragmented collateral fragment regenerates as a novel nucleus and co-grows with the principal dendritic branch. The molten dendrites undergo regeneration. According to the principle of minimum free energy, the lateral branch fragments are observed to form nuclei with an approximately spherical crystal structure. At the beginning of growth, adjacent dendrite fragments commence fusion, while the main dendritic branches gradually expose their tips, and the crystalline structure thickens significantly, as shown in Figure 6b.

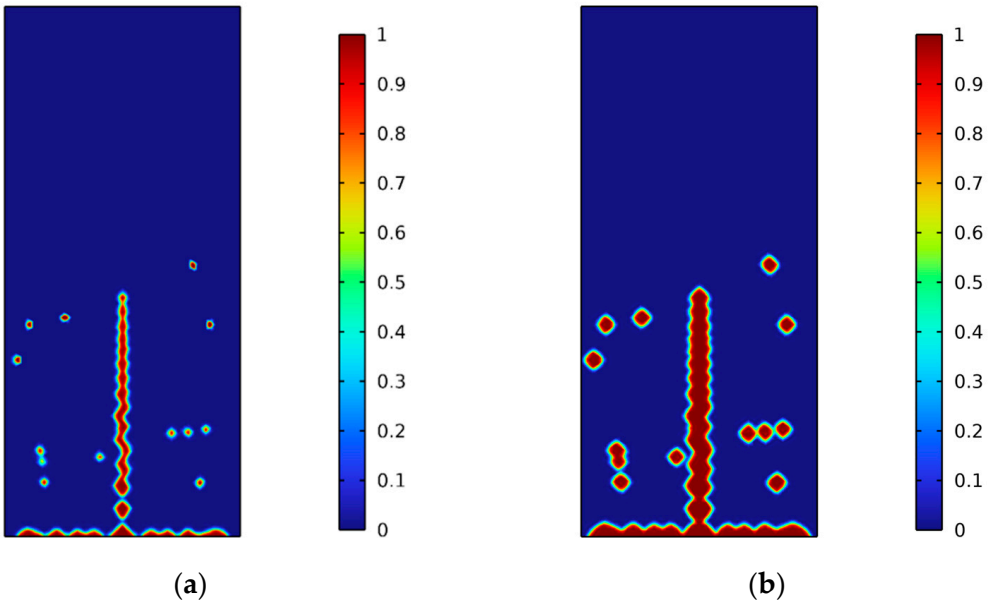

Figure 6. Dendrite morphology of lateral branches that were not completely melted and began to regenerate; (**a**) dendrite morphology at 0 Δt; and (**b**) dendrite morphology at 50 Δt.

The main axis of the dendrites no longer thickens at 100 Δt; instead, small protrusions emerge, and lateral branch fragments exhibit preferential growth due to interface anisotropy. At the same time, collateral debris near the main axis inhibits the coarsening of the main dendrite arms, as shown in Figure 7a. The presence of collateral debris in close proximity to the main axis hinders the coarsening process of the main dendrite arms, as shown in Figure 7a. The growth of dendrite tips and secondary dendrite arms becomes

significant at 200 Δt. Certain adjacent collateral fragments engage in competitive growth, while others undergo merging during the process. The presence of lateral dendrite debris adjacent to the main dendrite arm hinders the growth of the secondary dendrite arm and facilitates the thinning of the main dendrite, as shown in Figure 7b. The growth of the dendrite main axis is influenced by the competitive growth of neighboring dendrites at 500 Δt, leading to uneven characteristics in the growth of secondary dendrite arms. Simultaneously, these collateral fragments mutually impeded each other's growth during their competitive process, resulting in a substantial disparity in the growth rates of distinct collateral fragments, as shown in Figure 7c. At 1000 Δt, the dendrites complete the growth process in a limited space. The lateral branches of the principal dendrite, in conjunction with the main axis, give rise to a novel columnar crystalline structure. Meanwhile, a diverse range of dendrite morphologies was observed in the lateral dendritic fragments below the tip, indicating competitive interactions among dendrites (Figure 7d).

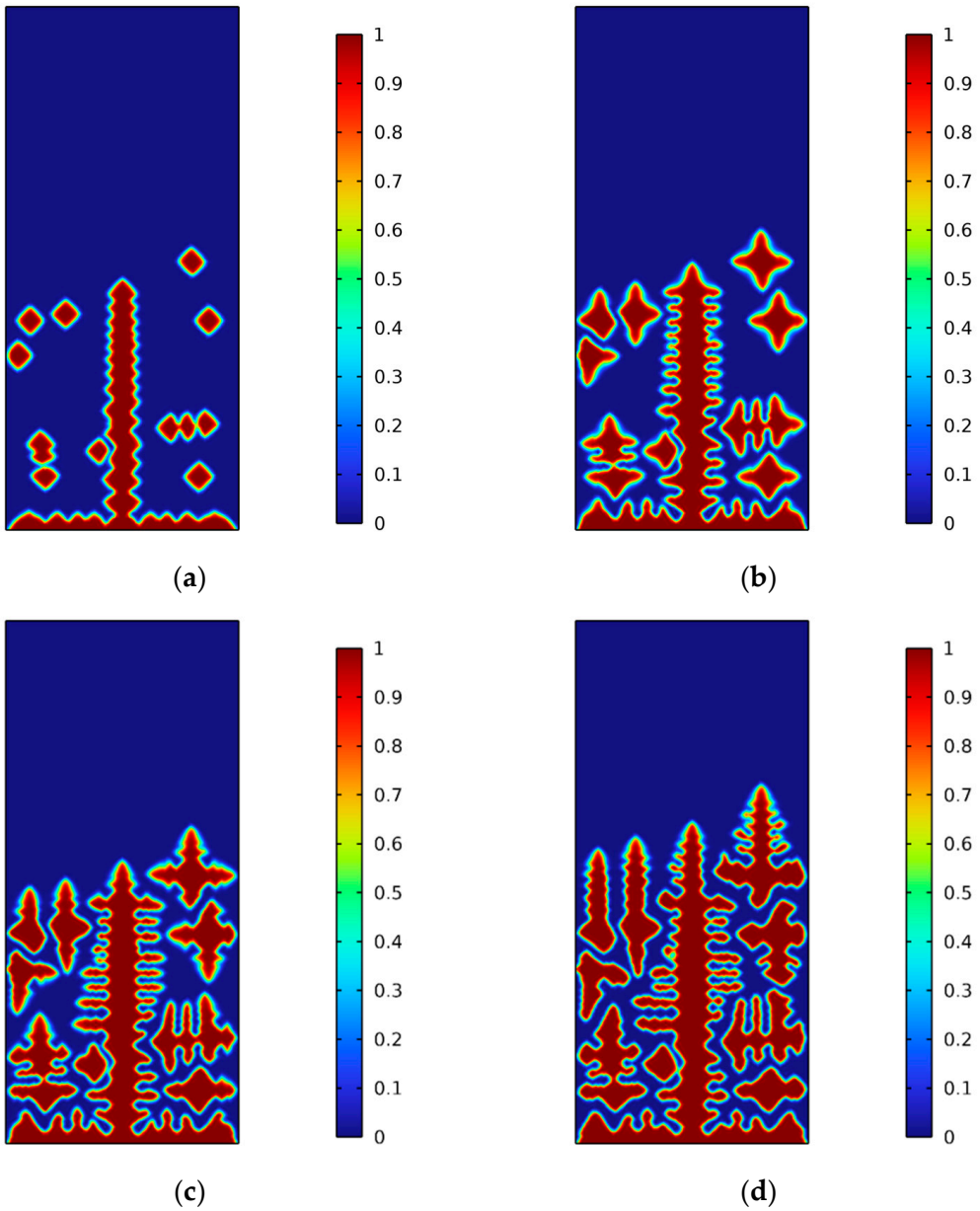

Figure 7. Microstructure refinement process of dendrite regrowth by remelting; (**a**) dendrite morphology at 100 Δt; (**b**) dendrite morphology at 200 Δt; (**c**) dendrite morphology at 500 Δt; and (**d**) dendrite morphology at 1000 Δt.

As shown in Figures 6 and 7, during the remelting dendrite regrowth process, the fragmented collateral pieces serve as novel crystal nuclei, thereby augmenting the nucleation count within the molten state. The competitive growth between these nuclei influences the crystal size, leading to a diverse range of crystal morphologies, thereby refining the microstructure during metal solidification.

5.3. Dendrite Regrowth Process in Which the Main Dendrites Are Not Completely Melted

During the dendrite remelting process, distinct thinning characteristics are observed in the main dendrite arms with varying degrees of melting. To provide a more comprehensive understanding of this process, this paper examines two representative models for dendrite regrowth and their subsequent refinement processes. The first is the regrowth process of partial melting fracture of the main dendrite arm, as shown in Figures 8 and 9. The second is the re-growth process of the main dendrite arm after a multi-stage melting fracture, as shown in Figures 10 and 11.

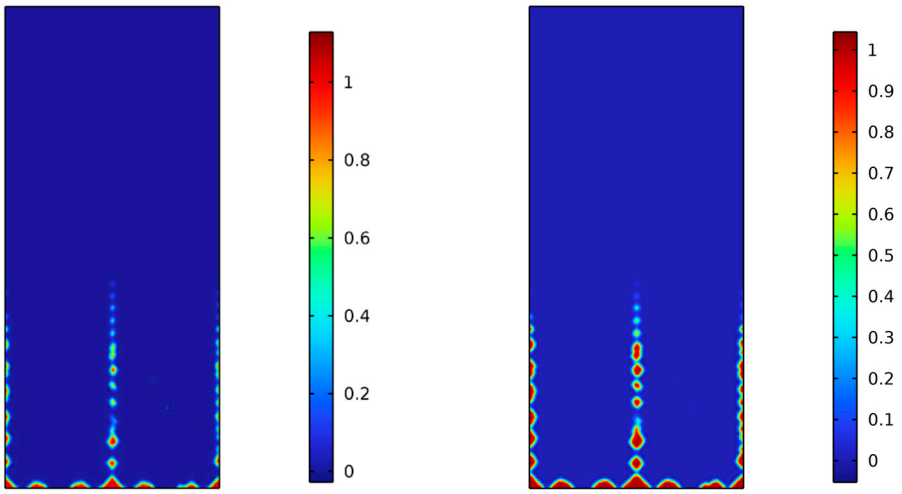

(**a**) (**b**)

Figure 8. Dendrite morphology of main dendrites that did not completely melt and began to regenerate; (**a**) dendrite morphology at 0 Δt; and (**b**) dendrite morphology at 20 Δt.

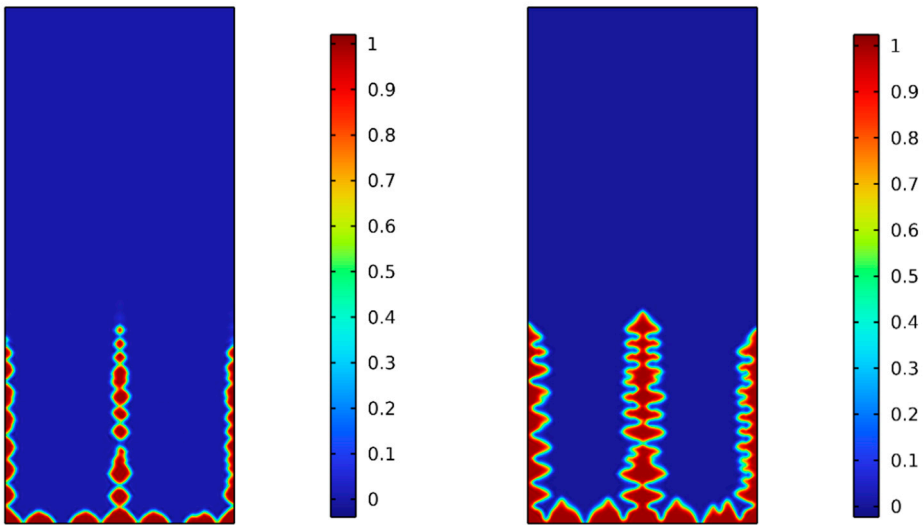

(**a**) (**b**)

Figure 9. *Cont.*

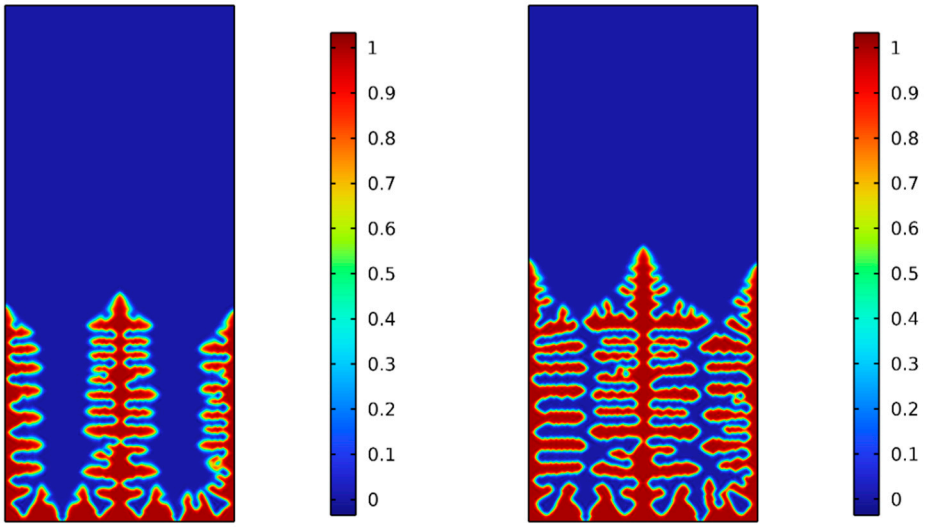

Figure 9. Microstructure refinement process of main dendrite regrowth by remelting; (**a**) dendrite morphology at 50 Δt; (**b**) dendrite morphology at 200 Δt; (**c**) dendrite morphology at 400 Δt; and (**d**) dendrite morphology at 1000 Δt.

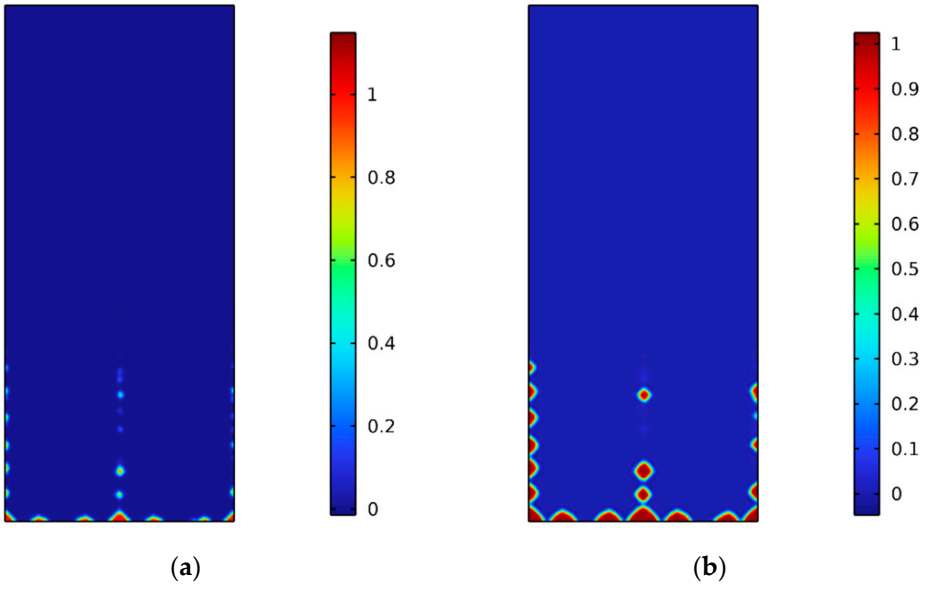

Figure 10. Main dendrite fragments and the morphologies of dendrites beginning to regrow; (**a**) dendrite morphology at 0 Δt; and (**b**) dendrite morphology at 50 Δt.

The lateral branches of the dendrites have undergone complete melting under temperature induction. The main dendrites exhibited partial fracture and melting, progressing from the tip to the root, as shown in Figure 8a. At 20 Δt, the fragmented sections of the main dendrites underwent a rapid transformation into novel nuclei, as shown in Figure 8b.

The regrowth process at 50 Δt is shown in Figure 9a. The newly formed crystal nuclei on the right undergo thermal-driven fusion, resulting in the formation of a new main dendrite arm, while the other two polycrystalline nuclei exhibit distinct growth characteristics. The nuclei of the three main dendrite fragments have undergone growth and fusion, resulting in the formation of new main dendrite arms at 200 Δt, as shown in Figure 9b. This is attributed to the newly fractured state of the main dendrite fragments, which imposes spatial constraints on crystal nucleus growth. During the early stage of incomplete nucleus growth, the competitive process intensifies to facilitate dendrite fusion.

At 400 Δt, the newly grown lateral branches of the main dendrites appear in two forms: one is the lateral branches of the new main dendrite arms, which appear late and are relatively thin. The other comprises the lateral branches resulting from the fusion of newly formed crystal nuclei, which exhibit a significant prominence during fusion and, therefore, possess relatively substantial thickness, as shown in Figure 9c. The new dendrites are fully grown at 1000 Δt. Before gravity melting, the dry crystal width of the main dendrites exhibited a significant reduction, while the growth of lateral dendrites appeared more uniform and coarser compared to before remelting, as shown in Figure 9d. The dendrites of this structure exhibit exceptional mechanical stability, thereby mitigating the occurrence of cracks during the solidification process.

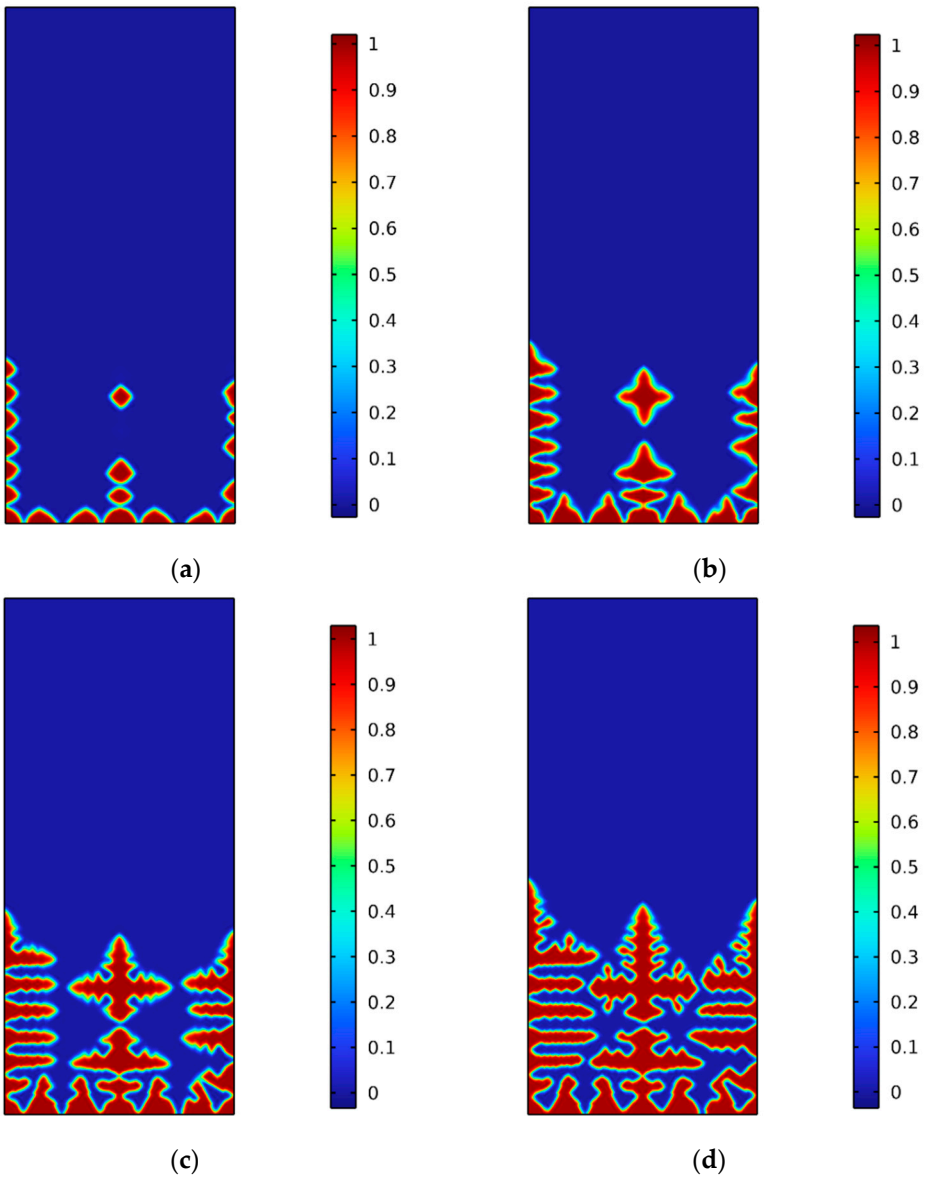

Figure 11. Multinucleate regrowth of main dendrite fragments; (**a**) dendrite morphology at 100 Δt; (**b**) dendrite morphology at 300 Δt; (**c**) dendrite morphology at 600 Δt; and (**d**) dendrite morphology at 1000 Δt.

In conjunction with Figures 8 and 9, the dendrite regrowth process exhibited no alterations in the morphology and structure of the dendrites as a result of the amalgamation and proliferation of novel crystal nuclei. The impact of this process on the microscopic

characteristics of dendrites primarily manifests as a reduction in the width of the main axis and an enhancement in the uniformity and alignment of the lateral branches.

In the remelting process, the majority of fragments resulting from the fracture of main dendrites have undergone complete melting, while the remaining components consist of unmelted dendrite fragments and main dendrite nuclei, as shown in Figure 10a. During the regrowth process at 50 Δt, the fragmented segments of the main dendrites underwent rapid metamorphosis into novel nuclei while concurrently initiating the growth of the main dendrite nuclei, as shown in Figure 10b.

Under the influence of ample growth space, supercooling-induced driving force, and interfacial anisotropy, the newly formed nuclei originating from dendrite fragments exhibit rapid growth. The growth characteristics of new nuclei at this stage exhibit a diverse range, as shown in Figure 11a,b. The crystal nuclei on both sides of the boundary show the growth trend of columnar crystals along their normal direction, while the crystal nuclei in the central region show the growth trend of equiaxial crystals. The number of crystal nuclei at the bottom also increased significantly compared to the initial state. The dendrites have fully grown during the regrowth process, spanning from 600 Δt to 1000 Δt. At this stage, the newly formed nuclei on both sides develop into columnar crystals aligned with the normal direction of the boundary. The equiaxed crystals near the bottom in the central region are limited by the bottom dendrites and the top dendrites, and the lateral dendrites in the horizontal direction are coarse and irregular equiaxed crystals. The equiaxed crystals located far from the bottom are constrained by both the horizontal and underlying dendrites, resulting in their growth into irregular equiaxed crystals that adopt an "inverted cross" shape, as shown in Figure 11c,d.

In conjunction with Figures 10 and 11, it is evident that the formation of new crystal nuclei enhances dendrite proliferation, leading to a significantly refined dendritic structure compared to the initial state characterized by three coarse columnar crystals. The growth process of the new nucleus exhibits anisotropy, leading to a transformation in the dendrite structure from columnar to equiaxial and a more intricate alternation between columnar growth structures. This process not only elucidates the microscopic dynamic changes occurring during dendrite remelting and regrowth but also unveils the impact of dendrite remelting on microstructure refinement. The thinning phenomenon leads to an increase in the number of crystals, thereby enhancing the overall material properties.

5.4. Dendrite Regrowth Process in Which the Main Dendrites Are Completely Melted

The dendritic structure near the cavitation center within the molten pool can undergo complete melting under instantaneous high temperatures. The cavitation effect generates an instantaneous high pressure, resulting in a corresponding increase in the melting point of the alloy. The subcooling degree of the melt in the local area is enhanced, thereby promoting the nucleation rate during the regrowth process of molten dendrites. At 3095 Δt, the dendrites were almost entirely melted, leaving only the roots with their original crystal nuclei and some fragments of unmelted dendrites, as shown in Figure 12a. After undergoing melting, the dendrites undergo a re-crystallization process at a new supercooling condition, serving as the initial stage of dendrite regrowth. As a result of the increased number of initial nuclei, the dendrite structure exhibits enhanced compactness during regrowth. Moreover, its growth direction becomes more distinct, and the occurrence of the "necking" phenomenon at the dendrite root is mitigated, as shown in Figure 12a–d.

The partial dendrite appearance of the cladding layer under ultrasonic vibration is shown in Figure 13. As shown in Figure 13a, it is evident that the lateral branches of columnar crystal 1 have undergone fracture, leading to the formation of novel crystals originating from these fragmented branches. The secondary dendrite arms of the main axis of columnar crystal 1 exhibit non-uniform growth characteristics, which aligns with the findings obtained through numerical simulation, as shown in Figure 7b. The upper part of the spindle in columnar crystal 2 exhibits a significant refinement compared to the lower part, as evident from Figure 13b. This observation is consistent with the findings presented

in Figure 9b of our main numerical simulation and further validates the established model proposed in this paper.

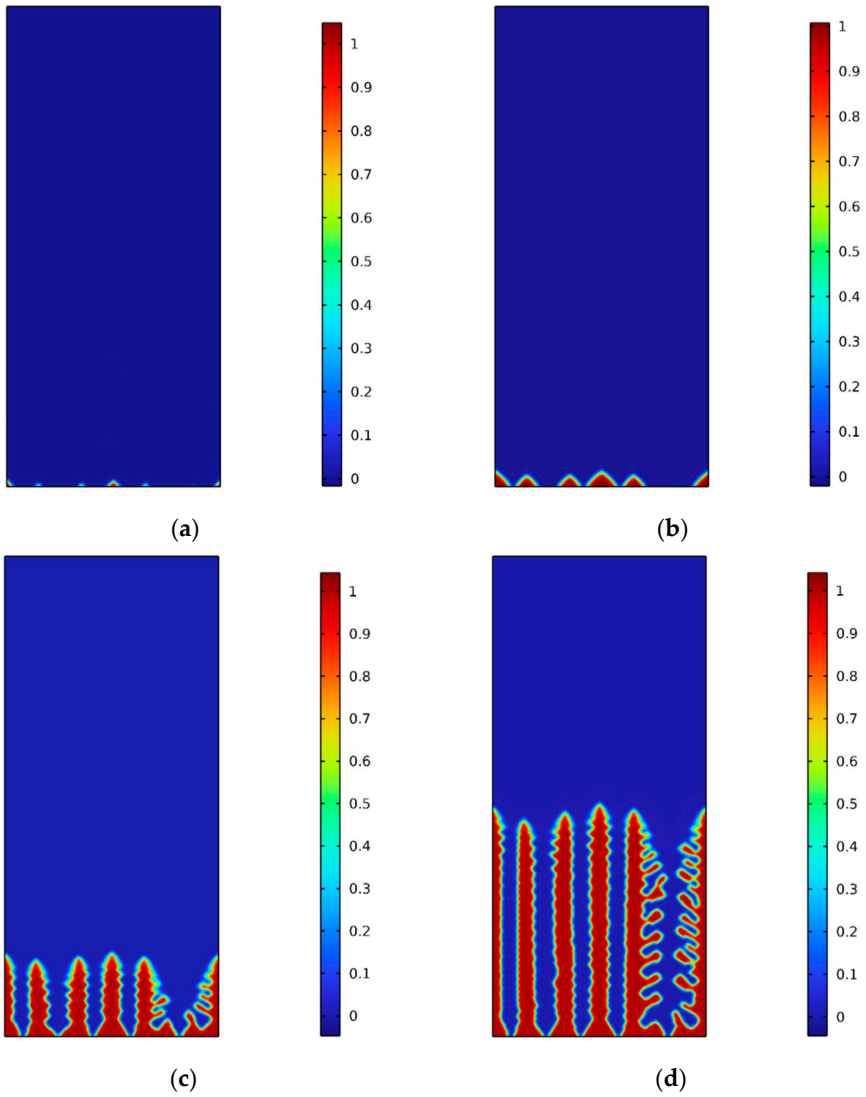

Figure 12. Morphology of dendrites regenerated by dendrite fragments and crystal nuclei; (**a**) dendrite morphology at 0 Δt; (**b**) dendrite morphology at 100 Δt; (**c**) dendrite morphology at 1000 Δt; and (**d**) dendrite morphology at 3000 Δt.

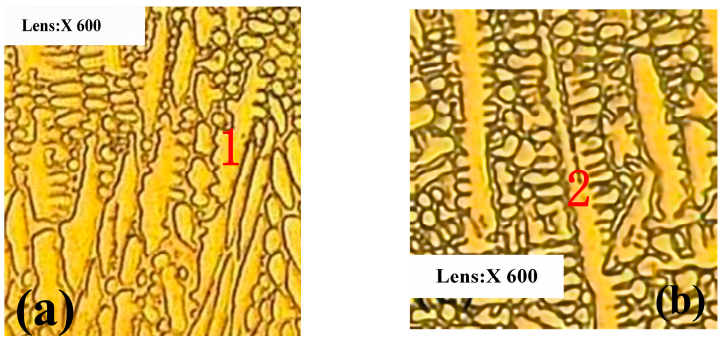

Figure 13. Microstructure of the cladding layer under ultrasonic vibration. (**a**) Heterogeneous microstructure of secondary dendrite arms. (**b**) Locally refined microstructure of the main dendrite arm.

6. Conclusions

(1) The calculation shows that the dendrite remelting process has a certain sequence: the lateral branches melt first, and the main dendrites melt later. When the lateral branches are not completely melted, and the root is not broken, the main dendrites can shrink to a certain extent but cannot melt.

(2) During the dendrite remelting process, two distinct modes of lateral branch melting can be observed: firstly, the root of the lateral branches fractures and gives rise to dendritic fragments during their contraction towards the main dendrite, predominantly occurring on well-developed lateral branches; secondly, the shorter growing lateral branches retract back to the main dendrites before fracturing.

(3) The main dendrite melting process, attributed to the heterogeneity of crystal structure and variations in lateral branch melting fracture, manifests as a multi-stage fracture phenomenon.

(4) The regrowth process can be primarily categorized into three scenarios through simulating dendrite regeneration under varying degrees of melting. In the first scenario, the lateral branch fragments give rise to new nuclei, which subsequently regenerate alongside the unmelted main dendrites, thereby augmenting both the number of crystals in the original region and the structural integrity of these newly formed crystals, consequently enhancing the microstructural characteristics. In the second scenario, diverse forms of regrowth processes for the main dendrite fragments after nucleation are observed based on competitive growth results. An improved solidification microstructure can be achieved by optimizing the morphology of the main dendrite arms, enhancing crystal quantity, and refining the crystal structure. The primary dendrites in the third case undergo complete melting, and the subsequent regrowth process enhances the number of initial nuclei, thereby refining the solidified microstructure without altering the original dendrite structure.

Author Contributions: C.L. acquired the grant and revised the paper; S.L. and J.L. performed modeling and wrote the paper; Y.S. extracted and analyzed the data; Y.W. and F.K. checked the grammar. All authors have read and agreed to the published version of the manuscript.

Funding: This work was supported by the Applied Basic Research Program of Liaoning Province (2023JH2/101300226), Liaoning Province Metallurgical equipment and process control key laboratory open project (2024KFKT-01), Liaoning Supported by the Fundamental Research Funds for the Liaoning Universities (LJ222410146021), Project for Graduate Education Reform and Technological Innovation and Entrepreneurship of University of Science and Technology Liaoning (2023YJSCX02).

Institutional Review Board Statement: Not applicable.

Informed Consent Statement: Not applicable.

Data Availability Statement: The data that supports the findings of this study are available within the article.

Conflicts of Interest: The authors declare no conflict of interest.

References

1. Ren, N.; Li, J.; Bogdan, N.; Xia, M.; Li, J. Simulation of dendritic remelting and fragmentation using coupled cellular automaton and Eulerian multiphase model. *Comput. Mater. Sci.* **2020**, *180*, 109714. [CrossRef]
2. Chuai, S.; Zhu, X.; Ye, L.; Liu, Y.; Wang, Z.; Li, F. Study on the mechanism of ultrasonic cavitation effect on the surface properties enhancement of TC17 titanium alloy. *Ultrason. Sonochem.* **2024**, *108*, 106957. [CrossRef]
3. Balasubramani, N.; Venezuela, J.; StJohn, D.; Wang, G.; Dargusch, M. A review of the origin of equiaxed grains during solidification under mechanical stirring, vibration, electromagnetic, electric-current, and ultrasonic treatments. *J. Mater. Sci. Technol.* **2023**, *144*, 243–265. [CrossRef]
4. Ning, F.; Cong, W. Ultrasonic vibration-assisted (UV-A) manufacturing processes: State of the art and future perspectives. *J. Manuf. Process.* **2020**, *51*, 174–190. [CrossRef]
5. Rayleigh, L., VIII. On the pressure developed in a liquid during the collapse of a spherical cavity. *Lond. Edinb. Dublin Philos. Mag. J. Sci.* **1917**, *34*, 94–98. [CrossRef]

6. Frenzel, H.; Schultes, H. Luminescenz im ultraschallbeschickten Wasser. *Z. Phys. Chem.* **1934**, *27*, 421–424. [CrossRef]
7. Noltingk, B.E.; Neppiras, E.A. Cavitation produced by ultrasonics. *Proc. Phys. Soc. Sect. B* **1950**, *63*, 674. [CrossRef]
8. Liang, J.; Wu, X.; Qiao, Y. Dynamics of twin bubbles formed by ultrasonic cavitation in a liquid. *Ultrason. Sonochem.* **2021**, *80*, 105837. [CrossRef]
9. Suslick, K.S.; Eddingsaas, N.C.; Flannigan, D.J.; Hopkins, S.D.; Xu, H. The chemical history of a bubble. *Acc. Chem. Res.* **2018**, *51*, 2169–2178. [CrossRef]
10. Zhong, X.; Eshraghi, J.; Vlachos, P.; Dabiri, S.; Ardekani, A.M. A model for a laser-induced cavitation bubble. *Int. J. Multiph. Flow* **2020**, *132*, 103433. [CrossRef]
11. Yamamoto, T. Bubble shape instability of acoustic cavitation in molten metal used in ultrasonic casting. *Ultrason. Sonochem.* **2024**, *111*, 107064. [CrossRef] [PubMed]
12. Zhao, Y.; He, W.; Yang, Y.; Liu, H.; Wei, Q.; Lin, B.; Song, D.; Sun, Z.; Zhang, W. Effect of ultrasonic treatment and squeeze casting on the microstructural refinement of Al–Cu–Mn alloys. *Int. J. Met.* **2024**, *18*, 869–881. [CrossRef]
13. Zhang, L.; Li, X.; Li, R.; Jiang, R.; Zhang, L. Effects of high-intensity ultrasound on the microstructures and mechanical properties of ultra-large 2219 Al alloy ingot. *Mater. Sci. Eng. A* **2019**, *763*, 138154. [CrossRef]
14. Ji, F.; Hu, Z.; Qin, X.; Yin, F.; Ni, M.; Xiong, X. Grain refinement and mechanism of steel in ultrasound assisted wire and arc additive manufacturing. *Int. Commun. Heat Mass Transf.* **2023**, *143*, 106724. [CrossRef]
15. Mullins, W.W.; Sekerka, R.F. Morphological stability of a particle growing by diffusion or heat flow. *J. Appl. Phys.* **1963**, *34*, 323–329. [CrossRef]
16. Liang, C.; Yin, Y.; Wang, W.; Yi, M. A thermodynamically consistent non-isothermal phase-field model for selective laser sintering. *Int. J. Mech. Sci.* **2023**, *259*, 108602. [CrossRef]
17. Shao, L.; Chen, B.; Yang, W.; He, J.; Tan, J. Numerical Modeling of Ice Crystal Dendritic Growth with Humidity by Using an Anisotropic Phase Field Model. *Cryst. Growth Des.* **2024**, *24*, 1400–1409. [CrossRef]
18. Azizi, G.; Kavousi, S.; Zaeem, M.A. Interactive effects of interfacial energy anisotropy and solute transport on solidification patterns of Al-Cu alloys. *Acta Mater.* **2022**, *231*, 117859. [CrossRef]
19. Al Azad, A.R.; Cardiff, P.; Browne, D.J. Development and Numerical Testing of a Model of Equiaxed Alloy Solidification Using a Phase Field Formulation. *Metals* **2023**, *13*, 1916. [CrossRef]
20. Zeng, H.B.; Ai, X.G.; Chen, M.; Hu, X.D. AApplication of phase field model coupled with convective effects in binary alloy directional solidification and roll casting processes. *Front. Mater.* **2022**, *9*, 989040. [CrossRef]
21. Ji, H.S.; Song, Q.H.; Du, Y.C.; Liu, Z.Q. Pseudorandom modeling and simulation of grain size of Inconel-718 microcomponent. *J. Mech. Eng.* **2023**, *59*, 232–240.
22. Long, W.; Cai, Q.; Chen, L.; Wei, B. Phase field simulation of dendrite growth in non-isothermal solidification of binary alloys. *Cast* **2003**, *52*, 695–699.
23. Rajkumar, V.; Du, Y.; Zeng, Y.; Tang, S. Phase-field simulation of solidification microstructure in Ni and Cu–Ni alloy using the Wheeler, Boettinger and McFadden model coupled with the CALPHAD data. *Calphad* **2020**, *68*, 101691. [CrossRef]
24. Kobayashi, R. Modeling and numerical simulations of dendritic crystal growth. *Phys. D Nonlinear Phenom.* **1993**, *6*, 410–423. [CrossRef]
25. Boettinger, W.J.; Warren, J.A.; Beckermann, C.; Karma, A. Phase-field simulation of solidification. *Annu. Rev. Mater. Res.* **2002**, *32*, 163–194. [CrossRef]
26. Zaeem, M.A.; Yin, H.; Felicelli, S.D. Modeling dendritic solidification of Al–3% Cu using cellular automaton and phase-field methods. *Appl. Math. Model.* **2013**, *37*, 3495–3503. [CrossRef]
27. Acharya, R.; Sharon, J.A.; Staroselsky, A. Prediction of microstructure in laser powder bed fusion process. *Acta Mater.* **2017**, *124*, 360–371. [CrossRef]